Phase-space resolved measurement of 2nd harmonic ion cyclotron heating using FIDA tomography at the ASDEX Upgrade tokamak

M. Weiland[1], R. Bilato[1], B. Geiger[1], P. A. Schneider[1], G. Tardini[1], M. Garcia-Muñoz[2], F. Ryter[1], M. Salewski[3], H. Zohm[1], the ASDEX Upgrade team and the EUROfusion MST1 team*

[1]Max-Planck-Institut für Plasmaphysik, 85748 Garching, Germany
[2]FAMN Department, Faculty of Physics, University of Seville, 41012 Seville, Spain
[3]Technical University of Denmark, Department of Physics, Dk-2800 Kgs. Lyngby, Denmark

Corresponding author: markus.weiland@ipp.mpg.de

Abstract

Recent upgrades to the FIDA (fast-ion D-alpha) diagnostic at ASDEX Upgrade allow to reconstruct the fast-ion phase space at several radial positions with decent energy and pitch resolution. These new diagnostic capabilities are applied to study the physics of 2nd harmonic ion cyclotron heating, which is a foreseen heating scenario for ITER. In particular, the acceleration of deuterium beam ions above the injection energy by absorption of ion cyclotron waves at the 2nd harmonic is investigated and compared to theoretical predictions by the TORIC-SSFPQL and TORIC-NUBEAM code packages. Furthermore, comparisons to other fast-ion diagnostics (neutron yield and neutral particle analyzers) are discussed.

1 Introduction

The absorption of radio frequency (RF) waves by ions is an important physics aspect for future fusion devices. In ITER, 2nd harmonic ion cyclotron resonance heating (ICRH) of tritium is one of the foreseen ICRH schemes, along with He-3 minority heating [1]. The 2nd harmonic heating has the benefit that it can accelerate the main ion species directly. However, it is only efficient for ions with large Larmor radii with respect to the RF wavelength. In addition, He-3 is very expensive, such that its usage must be reduced to an absolute minimum (e.g. for the plasma start-up phase, when the ions are cold and Larmor radii are small). Thus, it is important to understand the physics of 2nd harmonic heating for the success of future fusion devices such as ITER.

At ASDEX Upgrade (AUG), the Larmor radii of D beam ions, i.e. from 60 keV neutral beam injection (NBI), are large enough for effective 2nd harmonic absorption. For

*See the author list of "Overview of progress in European Medium Sized Tokamaks towards an integrated plasma-edge/wall solution" by H. Meyer et al., to be published in Nuclear Fusion Special issue: overview and summary reports from the 26th Fusion Energy Conference (Kyoto, Japan, 17-22 October 2016)

example, the beam ions from 60 keV neutral beam injection (NBI) have Larmor radii r_L of about 1.8 cm under a toroidal field of 2.4 T. Multiplied with the perpendicular RF wave vector, this results in a product of approximately $k_\perp r_\mathrm{L} \approx 0.72$ which is well above zero. Hence, 2$^{\mathrm{nd}}$ harmonic absorption can be studied by experimental investigation of the acceleration of those beam ions. This has already been demonstrated at many tokamaks [2, 3, and references therein]. Many measurements of the ICRH acceleration have been carried out using neutral particle analyzers [4] or measurement of the neutron rates created by D-D fusion. In addition, neutron spectroscopy has become a valuable tool [5, 6], because the neutron energy spectrum yields information about the velocity distribution of the initial fusion reactants (i.e. the deuterium ions). Fast ions that are so strongly accelerated by ICRH, such that their orbits are no longer confined, can be measured with fast-ion loss detectors [7, 8]. In addition, gamma-ray measurements [9, 10] and collective Thomson scattering [11] have been used to detect ion acceleration by ICRH.

With the FIDA diagnostic, observations of beam-ion acceleration by ICRH harmonics have been reported at DIII-D [3] and NSTX [12]. The FIDA diagnostic has the advantage that it can provide both a very well spatially localized measurement and a decent velocity space resolution. Recently, the FIDA diagnostic at ASDEX Upgrade [13, 14] has been upgraded towards five viewing directions to allow even a tomographic reconstruction of the 2D velocity space distribution at several well-defined spatial measurement positions [14–16]. In previous work [14], it has been demonstrated that FIDA tomography is well able to distinguish between 60 and 93 keV NBI. Hence, the diagnostic capabilities allow to measure ICRH-induced acceleration of 60 keV NBI above the injection energy. In this paper, we present the first observations of 2$^{\mathrm{nd}}$ harmonic beam ion acceleration with FIDA tomography. These results are then compared to theoretical predictions by TORIC-SSFPQL [17–21] and TORIC/TRANSP [22–25].

2 Preliminary considerations on FIDA data

At the 2$^{\mathrm{nd}}$ harmonic ICRH resonance of deuterium, hydrogen is also resonant at the fundamental cyclotron frequency. The hydrogen concentration cannot be controlled directly. At ASDEX Upgrade, a typical hydrogen concentration of 5% is present in the machine, which is measured by mass-separated neutral particle analyzers [26]. This gives rise to hydrogen minority ICRH heating, which is in competition with 2$^{\mathrm{nd}}$ harmonic absorption by D beam ions.

For of the FIDA diagnostic, the resulting fast-hydrogen distribution F_H has to be considered, because the H_α line ($\lambda_{0,\mathrm{H}} = 656.28$ nm) lies very close to the D_α line $\lambda_{0,\mathrm{D}} = 656.10$ nm. Thus, the FIDA technique cannot distinguish between fast deuterium and fast hydrogen ions, but will measure a sum of both contributions. To assess an upper bound of the H contribution in the presence of ICRH, the hydrogen distribution can be assumed to be entirely non-Maxwellian and hydrogen should then be considered entirely as fast-ion species. This must be compared to the fast D ion density, which has typical concentrations of 10%. Thus, we will further investigate the contribution of fast H to the FIDA signal.

To further quantify it, we have computed weight functions $W_{\mathrm{H,D}}$ both for hydrogen and deuterium with the FIDASIM code [27–29], which are defined such that the FIDA signal

is given by weighted integrals of the hydrogen and deuterium distribution functions $F_{\mathrm{H,D}}$:

$$FIDA(\lambda) = \iint W_{\mathrm{H}}(\lambda, E, \xi) F_{\mathrm{H}}(E, \xi) \mathrm{d}E \mathrm{d}\xi + \iint W_{\mathrm{D}}(\lambda, E, \xi) F_{\mathrm{D}}(E, \xi) \mathrm{d}E \mathrm{d}\xi \qquad (1)$$

The integration is carried out in the velocity space, for which we use the energy E and the pitch $\xi = v_{\parallel}/v$ as coordinates. The sign of the pitch is defined relative to the plasma current (i.e. $\xi > 0$ corresponds to the co-current direction). To calculate W_{H}, the FIDASIM code had to be slightly adapted, because it was used only for deuterium before. These adaptations were, however, straightforward: In particular, the cross-sections in the collisional radiative model are valid for all hydrogen isotopes, such that only the difference in the ion mass has to be considered. The calculation results for a Doppler-shift of 4.95 nm are shown in figure 1. It can be seen that the weight functions for H and D lie exactly on top of each other (both in shape and absolute values), when plotted as a function of pitch $\xi = v_{\parallel}/v$ and $E/m = v^2/2$. This can be understood easily: The

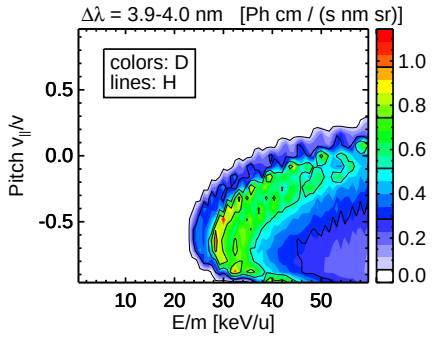

Figure 1: Comparison between weight functions for hydrogen and deuterium.

Doppler-shift is proportional to the velocity v (precisely: the projection of $\vec{v}$ onto the line of sight). In addition, all cross-sections considered by FIDASIM depend on the relative velocities between the reactants (charge exchange, ion-impact ionization/excitation and electron-impact ionization/excitation).

So, the weight functions for H and D are equal with respect to equal Doppler-shift $W_{\mathrm{H}}(\lambda - \lambda_{0,\mathrm{H}}) = W_{\mathrm{D}}(\lambda - \lambda_{0,\mathrm{D}})$. If the small difference between the H_α and D_α wavelength is neglected ($\lambda_{0,\mathrm{H}} \approx \lambda_{0,\mathrm{D}}$), the FIDA signal can be directly interpreted as a sum of the H and D fast-ion distribution functions:

$$FIDA(\lambda) \approx \iint W_{\mathrm{D}}(\lambda, \tfrac{E}{m}, \xi) \cdot \left(F_{\mathrm{H}}(\tfrac{E}{m}, \xi) + F_{\mathrm{D}}(\tfrac{E}{m}, \xi) \right) \mathrm{d}\tfrac{E}{m} \mathrm{d}\xi \qquad (2)$$

This assumption allows to calculate meaningful FIDA tomographies in the presence of both fast H and fast D. Hereby, it is important to calculate the tomography in terms of E/m (or v), which can then be interpreted as sum of H and D. Within this work, we will assume $\lambda_0 = \lambda_{0,\mathrm{D}}$. This means that the D contribution to the FIDA signal will be analyzed exactly, while the H contribution will enter into the tomography with an offset of 0.18 nm. Compared to the spectral resolution of the spectrometer (0.21 nm) and compared to the absolute value of analyzed Doppler-shifts ($\approx$ 3 nm - 7 nm) this is

acceptable. Furthermore, the H distribution is expected to have a rather smooth, almost bi-Maxwellian shape, for which such an offset is less important than for the D beam ion distribution.

3 FIDA tomography in the plasma center

We have analyzed discharge #30809, which features a toroidal field of $B_t = -2.4$ T and plasma current of $I_p = 1.0$ MA. The ICRH frequency is 36.5 MHz and the resonance layer is located at $R \approx 1.69$ m (neglecting Doppler shifts), i.e. very close to the magnetic axis. Representative time traces of the discharge are shown in fig. 2. The rather low electron density ($n_e \approx 3 \cdot 10^{19}$ m^{-3}) leads to low bremsstrahlung, which is very beneficial for the FIDA signal-to-background ratio. The plasma shows strong sawtooth oscillations with rather long periods in the range of 120 ms. The fast-ion redistribution due to sawteeth has already been investigated with the FIDA tomography in [14, 30, 31]. In order to have nearly steady-state conditions, we chose time points just before a sawtooth crash. We have compared $t = 4.60$ s with 2.4 MW NBI + 2.0 MW ICRH and $t = 4.48$ s with 2.4 MW NBI only (the time-points are indicated with dashed lines in fig. 2).

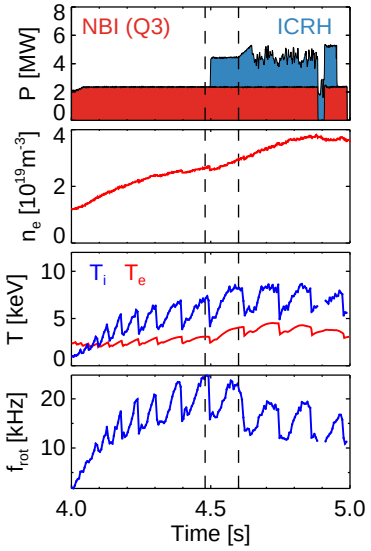

Figure 2: Representative timetraces for discharge #30809. The analyzed time points are marked with dashed lines.

FIDA data from four viewing arrays are available for this discharge. Figure 3 gives an overview of the FIDA measurement positions used for this analysis. The measurement position is determined by the overlap between the lines of sight and the neutrals from NBI source Q3 (calculated by FIDASIM). The local angle Φ between the magnetic field and the lines of sight is indicated by the color coding. In order to calculate a FIDA tomography, the measurements with different angle Φ at similar position are grouped together, as it is indicated by the boxes. In this section, we will discuss in detail the results of the FIDA tomography at the innermost box, and in section 5 we will discuss the profiles calculated from all measurement positions.

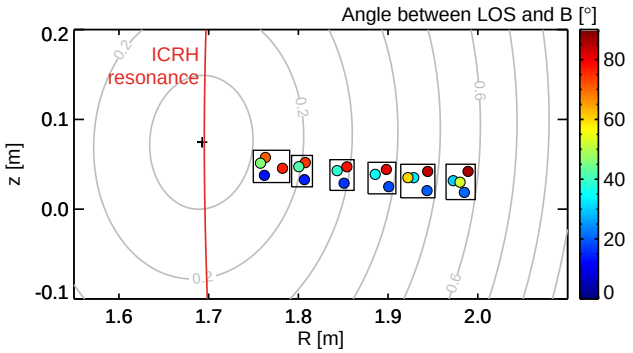

Figure 3: FIDA measurement points in the poloidal cross-section. Contours of ρ_{tor} are shown in grey lines (at 4.60s).

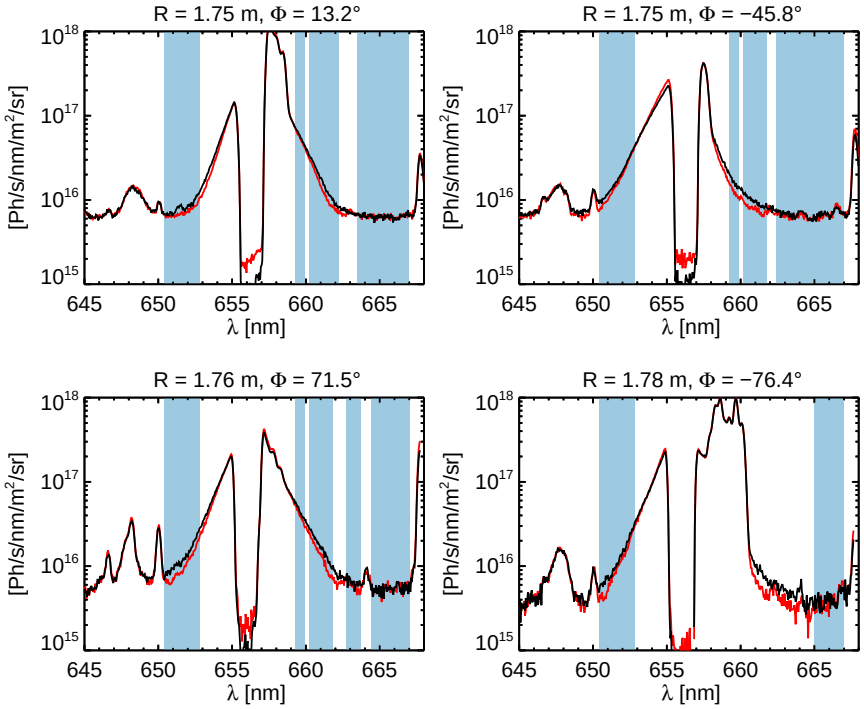

Figure 4: FIDA spectra of the four center-most lines of sight at $t = 4.48$s (NBI only, red line) and $t = 4.6$s (NBI+ICRH, black line). The tomography is calculated from the blue-shaded regions. The bright central D_α line (656.1 nm) is filtered by a wire [14]. The background level (due to bremsstrahlung) is is evaluated at 665-667 nm and it is slightly higher in the NBI+ICRH phase. To allow a better comparison of the spectral shapes, a similar level of bremsstrahlung is achieved by adding half of the difference to the NBI-only spectrum and substracting it from the NBI+ICRH spectrum. For the calculation of the tomography the bremsstrahlung is subtracted from each spectrum.

The spectra which are used for the inner-most tomography position are shown in fig. 4. A small offset has been added to the spectra to obtain a similar level of bremsstrahlung in the NBI-only and NBI+ICRH phase, allowing us to better compare the spectral shapes. Fast ions with the NBI injection energy (60 keV) can have a maximum Doppler-shift of

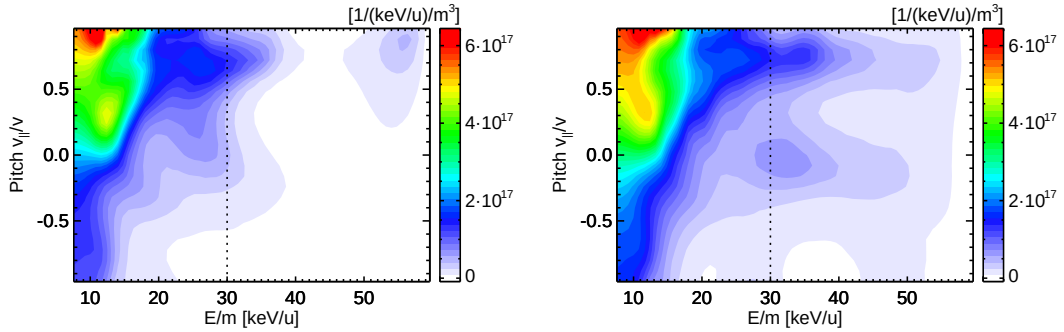

(a) 4.48s (NBI only) **(b)** 4.60s (NBI+ICRH)

Figure 5: FIDA tomography at $\rho_{\mathrm{tor}} = 0.12$ (on the low field side).

5.2 nm (neglecting Stark splitting), which corresponds to 661.3 nm on the right and 650.9 nm on the left side of the D-alpha line. In the NBI-only phase, FIDA light is measured only within these boundaries. In the NBI+ICRH phase, tails above these boundaries are visible, which indicates that fast ions above the injection energy are present and that the FIDA diagnostic is sensitive enough to measure them. An example, where this can be seen quite clearly, is the top-right spectrum ($\Phi = -45.8°$) at wavelengths around 660-661.5 nm (i.e. Doppler-shifts $\Delta\lambda$ of 3.9-5.4 nm). The weight function for the lower boundary ($\Delta\lambda$=3.9-4.0 nm) of this wavelength range has been shown already in figure 1). NBI source Q3 injects ions with 30 keV/u and positive pitches around 0.6, while the weight function indicates that this part of the spectrum is mostly sensitive to fast-ions with negative pitches (from -1 to 0) and energies around or above the NBI injection energy of 30 keV/u. Hence, this particular weight function does hardly intersect with the expected beam ion distribution (comp. also fig. 7) and instead, it is looking at a part of the velocity space where we can expect mostly ICRH accelerated ions. Thus, we expect a very low FIDA signal (i.e. close to the flat bremsstrahlung background) in the NBI-only phase, which is what the measurerement shows indeed (red curve). In the NBI+ICRH phase, we see a significant signal increase in the discussed wavelength range (660-661.5 nm) and further above (up to $\approx$ 663.5 nm).

The tomographic reconstruction of the velocity space is calculated from the blue-shaded areas (avoiding impurity lines). As tomography method, we use 1$^{\mathrm{st}}$ order Tikhonov regularization (which demands the solution to have small gradients) as described and successfully tested in [14]. This method includes also an iterative, strong damping of negative values, which is significantly faster than the rigid non-negativity constraint used in [31]. The background due to bremsstrahlung is assumed to be a flat line. It is evaluated at 665-667 nm and subtracted from the spectra. The result of the tomography is shown in fig. 5. Here, the NBI full injection energy (30 keV/u) is marked with a dashed line. In the NBI-only phase ($t = 4.48$ s), the tomography yields mainly fast ions with energies below the injection energy, as expected. Towards very high energies ($\gtrsim$50 keV/u), a small localized peak in the tomography is seen, which is most likely an artifact due to measurement noise or small impurity lines, as discussed later in section 5. In the presence of ICRH (4.60 s), two high energy tails are clearly seen. The stronger tail appears at pitches $\approx$ 0.7, and can be identified as beam ions, which have been further

accelerated by ICRH. The acceleration is in fact a velocity-space diffusion along the contours of $L = v_\perp^2 + (v_\parallel - \omega/k_\parallel)^2$ [32], with $v_\parallel$ to be taken in the lab frame, ω the RF angular frequency and $k_\parallel \approx 7\,\mathrm{m}$ at ASDEX Upgrade. To estimate the direction of diffusion, we have evaluated L at the resonance position, and then mapped it to the measurement position on the low field side, assuming conservation of magnetic moment and zero-orbit-width. The results of this "back-of-the-envelope" calculation are shown in fig. 6 as grey contour lines. This approximate calculation would in principle expect a slightly steeper slope of the high energy tail towards lower pitches. Within the limited pitch resolution of the tomography, this is however still a reasonable agreement. Also it must be kept in mind that this is only an strongly simplified calculation, and a comparison to more sophisticated theoretical models is carried out in section 4.

A second, weaker high energy tail is seen at pitches -0.3 to $+0.1$. Particles within this region are on trapped orbits, as shown in the orbit classification plot fig. 6. This

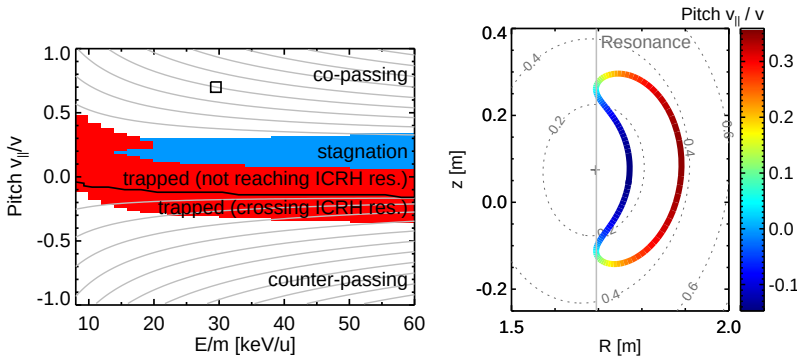

Figure 6: Left: Classification of the fast-ion orbits which pass through the measurement position ($\rho_{\mathrm{tor}} = 0.12$ on the low field side, in the lab frame). The orbits are calculated assuming a vanishing electric field in the plasma frame. Grey lines indicate the direction of RF induced diffusion/acceleration according to a simplified calculation (explained in the text). Right: Deuterium ion orbit corresponding to the second high energy tail ($E = 45\,\mathrm{keV/u}$, $\xi = -0.14$). Dashed lines show contours of ρ_{tor} and the grey line shows the ICRH resonance layer. The pitch $v_\parallel/v$ is shown in the lab frame, which is why the banana tips have $v_\parallel = v_{\mathrm{rot},\varphi}$ rather than $v_\parallel = 0$.

is in agreement with the well-known effect of "resonance localization" [33, 34]: ICRH increases dominantly the perpendicular velocity, which means that a given particle gets eventually pushed into the trapped region of the velocity space. This may continue, until the particle is so deeply trapped that it does not reach the ICRH resonance layer anymore. This leads to an accumulation of fast-ions in the corresponding velocity-space region, which is given by the boundary, where trapped particles have their banana tips at the resonance layer (see the right of fig. 6). Consequently, the high energy tails are located around that boundary. This effect is further enhanced by the low parallel velocity close to the banana tips, which means that these ions spend a larger fraction of their orbit within the resonance region and get accelerated more strongly. In fig. 6 (left), the velocity space location for trapped orbits, which have their banana tip at the resonance layer, is shown with the black line, and it coincides well with the second high energy tail in the tomography. This tail can originate both from hydrogen and deuterium, because both

species are subject to the resonance localization. In fact, for deuterium the resonance localization effect might be even stronger: The low $v_\parallel$ close to the banana tip goes along with high $v_\perp$ and hence large Larmor radii, which makes second harmonic absorption more effective. Concretely, this means that beam ions from further outside, where the trapping cone is larger and the beam ions are thus injected closer to the trapped-passing boundary, become trapped by interaction with the RF waves and then reappear on their inner banana leg (i.e. with negative pitches) at the measurement position. Even more further outside, beam ions are directly trapped from their birth, and the RF-acceleration could increase their banana widths such that they reappear in the plasma center. We can conclude that the tomography results are qualitatively in line with basic theoretical considerations.

4 Comparison with theory

4.1 Code overview

In the following, we turn to a quantitative comparison with predictions with the TORIC-SSFPQL code [17–21] and the TORIC Monte Carlo kick operator in TRANSP/NUBEAM [22–24]. TORIC-SSFPQL calculates the steady-state H and D distributions. The NBI source (i.e. the deposition) is calculated by SINBAD [18]. The main limitation of the code package is that the Fokker-Planck part SSFPQL assumes that ions move on flux surfaces (zero orbit width approximation). Within this approximation, an ad-hoc correction for particle trapping effects is included in the quasi-linear RF diffusion operator [35, 36].

The TRANSP/NUBEAM package delivers only the fast D (i.e. beam ion) distribution function. Here, all orbit effects are taken into account by a Monte Carlo approach, and the effect of 2^{nd} harmonic ICRH is modeled by applying kicks to the Monte Carlo markers during their pass through the resonance layer. With this approach, TRANSP is also able to model dynamical processes (not only the steady-state solution). It should be noted that the kick operator is still being developed and improved [25]. The TRANSP simulations presented in this paper where updated closely before the initial submission (December 2016) and the results differ slightly from an earlier version presented in [37]. Thermal deuterium ions are not considered in this Monte Carlo approach. To get the full D distribution function, we add the thermal D distribution modeled by a shifted Maxwellian (according to the measured ion temperature and plasma rotation). For hydrogen, a coupling between the TORIC and FFPMOD [34] codes is used. Here, only parallel and perpendicular temperatures are given in the output, such that we model the H distribution function with a bi-Maxwellian. The version of TORIC in TRANSP is based on the version TORICv5 [38, 39]. TORIC-SSFPQL uses the most recent version TORICv6 [20, 21], where TORIC accepts generic numerical distribution function for the evaluation of the coefficient of the wave equations.

For the comparison with the experimental results, we have to evaluate the fast-ion distribution function at the measurement position in the lab frame. For the calculation of the FIDA tomography we have grouped several lines of sight at slightly different locations (see fig. 3) and in addition, each of these lines of sight has a finite measurement volume [14]. We take this into account by calculating corresponding volume averages of the distribution function. For the TRANSP/NUBEAM output this is straightforward, because it

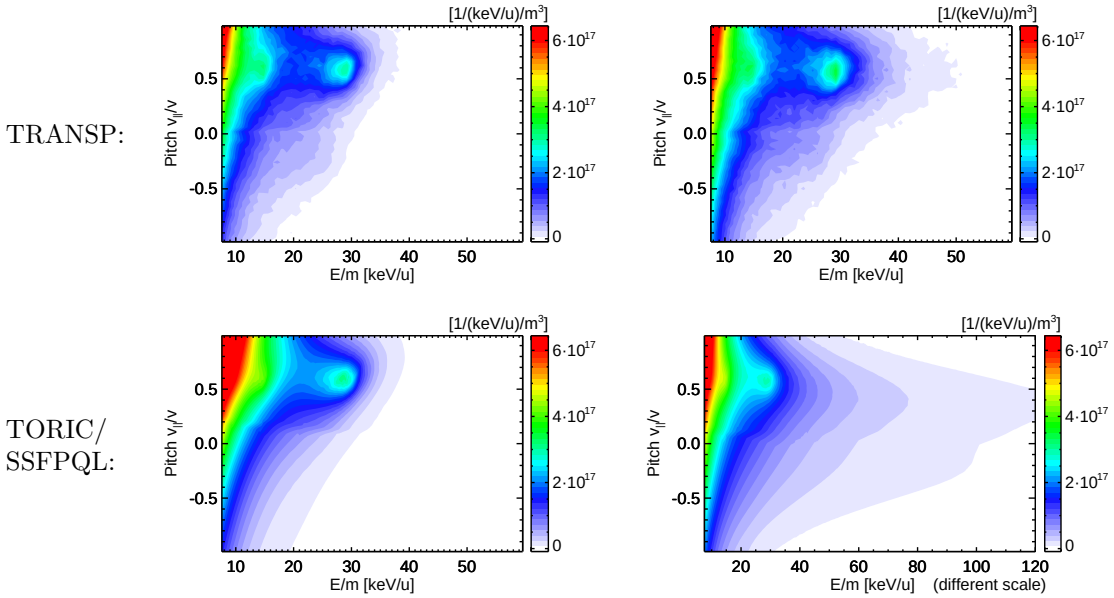

(a) 4.48s (NBI only) **(b)** 4.60s (NBI+ICRH)

Figure 7: Calculated D distribution functions by TRANSP (top row) and TORIC/SSFPQL (bottom row).

is already given on an 2D (R,z)-grid in the lab frame. The output of SSFPQL is given as a 1D radial profile on the outer midplane, and we perform a mapping onto a (R,z)-grid based on the conservation of the magnetic moment and the zero-orbit-width approximation (i.e. consistent with the assumptions made in SSFPQL). In TORIC/SSFPQL, plasma rotation is now considered both for ICRH absorption [40] and NBI (implemented for this paper). The output distribution function of SSFPQL is given in the plasma frame, and is then transformed into the lab frame for comparison with TRANSP and the experiment. Consequently, all plots in this paper are shown in the lab frame.

4.2 Deuterium

The calculated fast D distribution functions are shown in fig. 7 for both codes. In the NBI phase, reasonable agreement between both codes is seen. Due to the strong plasma rotation, the distribution function (in the lab frame) is tilted towards positive pitches, which can be seen quite clearly towards lower energies.

The FIDA tomography (fig. 5a) shows less pronounced peaks and a more smoothed out velocity distribution. This has been discussed already in previous analysis [14]. It can be explained as a feature of the 1st order Tikhonov regularization [41–43], which is used to calculate the tomography and which favors solutions with low gradients. Also it indicates the resolution limitations of the tomography. Since the peaks carry mostly geometric information about the NBI setup while the interesting physics aspects lie elsewhere in the velocity space, this is here an acceptable limitation [14, 37].

To provide a more quantitative comparison, we compute energy and pitch profiles (figures 8 and 9) by integrating out the other coordinate, respectively. Both energy and pitch profiles show good agreement. In the energy profile, we see again clearly that the

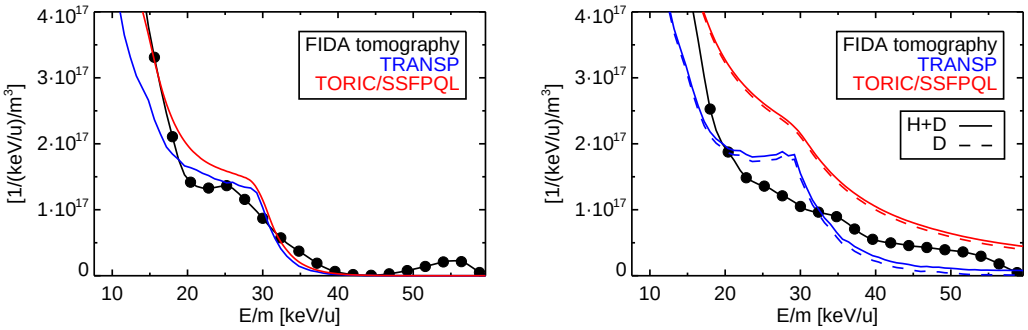

(a) 4.48s (NBI only) **(b)** 4.60s (NBI+ICRH)

Figure 8: Energy profiles $\int F(E/m, \xi)\mathrm{d}\xi$. Every third pixel of the tomographic reconstruction is plotted with a dot.

FIDA tomography tends to smooth the energy step at the highest injection energy (30 keV/u). In the simulation, this is a rather sharp step, with a very weak high-energy tail due to collisional velocity diffusion. In general, however, the absolute values between tomography and simulation match quite well, especially if one integrates over the region around the step. This can be seen in the pitch profile (fig. 9), for which we have integrated over E=25-60 keV/u. The NBI injection peak differs in the tomography by a shift of ≈ 0.1 in pitch, which is within the uncertainties of the tomographic reconstruction. Towards $\xi = 0$, a second small peak appears in the reconstruction, which could be explained by trapped particles.

When comparing the two codes, the pitch distributions have a similar shape. The slight discontinuity in the TORIC/SSFPQL result at $\xi \approx 0.12$ corresponds to $\xi \approx 0.0$ in the plasma frame and is a consequence of the mapping (necessary to determine the distribution function at the measurement volume) and the fact that the distribution function is not symmetric in the trapping cone with respect to the pitch ($F(E, -\xi) \neq F(E, \xi)$), as it would be expected in the zero-orbit-width approximation. The absolute values are slightly higher in SSFPQL, which could be partly caused by differences in the neutral beam attenuation cross-sections. In line with that, the beam shine-through is higher in NUBEAM (350 kW vs. 250 kW). In addition, the ions are assumed to stay on their initial flux surface in SSFPQL, while in NUBEAM, the orbits are treated realistically including radial collisional transport. This has of course also an influence of the radial profile shape, and could thus be also a reason for the difference in absolute values. A consequence of these orbit physics can be seen when looking closely at the pitch profile of TRANSP/NUBEAM: A distinct step can be seen around $\xi = -0.4$. On the right side of the step the NUBEAM result is slightly enhanced due to trapped fast ions. On the left side of the step, the pitch distribution drops to zero. This can be explained with the boundary between trapped and counter-passing ions (comp. fig. 6), which is also located at $\xi = -0.4$. The orbits of barely trapped orbits are very large banana orbits, which can be radially redistributed very strongly. Thus only very few ions manage to "make it" over that boundary, explaining the distinct step.

We turn now to the NBI+ICRH phase. Contour plots of the calculated D distribution function for the considered measurement position in the plasma center are shown

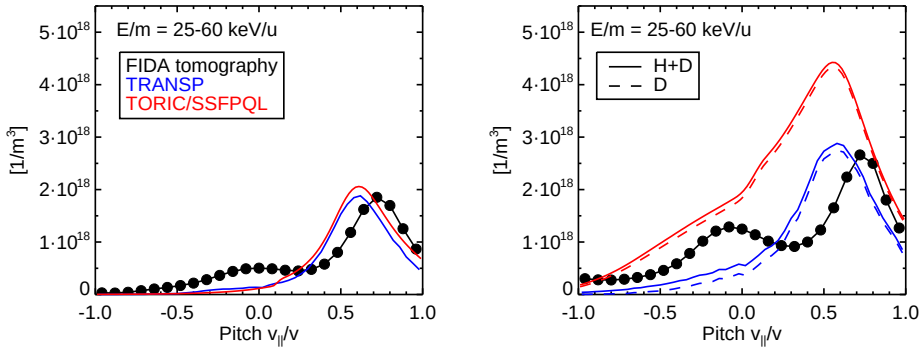

(a) 4.48s (NBI only) **(b)** 4.60s (NBI+ICRH)

Figure 9: Pitch profiles $\int_{25\ \mathrm{keV/u}}^{60\ \mathrm{keV/u}} F(\frac{E}{m}, \xi) \mathrm{d}\frac{E}{m}$.

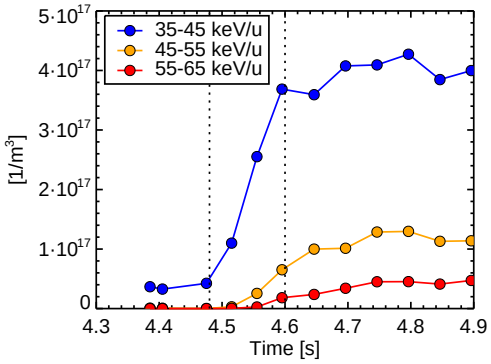

Figure 10: TRANSP prediction of the temporal evolution of the D fast-ion density at the central FIDA measurement position in various energy ranges above the NBI injection energy. In the TRANSP run, all inputs (e.g. kinetic profiles) are kept constant after 4.6 s to check if the D distribution is already close to steady state conditions.

in fig. 7b. TORIC-SSFPQL predicts much stronger second harmonic high energy tails than TRANSP. However, it predicts two high energy tails, a stronger close to the beam injection peak and a weaker one at negative pitches, which is in qualitative agreement with the FIDA tomography. The TRANSP high energy tail is situated at same pitch as the beam injection peaks, in accordance with the stronger high energy tail seen in the tomography. The high energy tail is rather flat with respect to the pitch, which is in better agreement with the tomography than the "back-of-the-envelope" calculation shown in fig. 6. A second high energy tail (as seen in the FIDA tomography) is hardly visible in the contour plot. In the pitch profile (fig. 9b), calculated by integration over the high-energy range (25 keV/u - 60 keV/u), it can be seen that TRANSP predicts at least a significant increase at $\xi \approx -0.1$ compared to the NBI only case. Thus, also TRANSP predicts an increased phase-space density corresponding to trapped fast ions with their banana tip close to the resonance, but this enhancement is smaller than in the FIDA tomography (and much smaller than in the TORIC/SSFPQL code).

In the energy profiles (fig. 8), the acceleration of beam ions is clearly seen in the FIDA tomography by a high energy tail. For comparison, the FIDA tomography goes to

zero at ≈ 40 keV/u in the NBI-only phase. The deuterium energy profile calculated by TRANSP and TORIC/SSFPQL are shown with dashed lines in blue and red, respectively. The TRANSP prediction is below the FIDA tomography, while the TORIC/SSFPQL is clearly too high. A possible explanation for this strong overprediction could be that the considered time point (4.6 s) is too close to the ICRH onset at 4.5 s, such that a steady state is not reached yet (as it is assumed by TORIC/SSFPQL). To check this, we have carried out a dedicated TRANSP run, where we keep the kinetic profiles and the heating power constant after 4.6 s (while they are evolving in reality) and deactivate the sawtooth model. The predicted temporal evolution of D fast-ion density at the measurement position are shown in fig. 10 for several energy intervals above the NBI injection energy. The analyzed time point (4.6 s) lies after the strong rise of the fast-ion density following the ICRH-onset at 4.5 s. In particular, the ion density in the lowest energy interval (from 35 to 45 keV/u) rises only very weakly after 4.6 s. Thus, the D distribution function is already very close to steady-state conditions (at least for the energy range most relevant for the FIDA diagnostic) - and the large overprediction by TORIC/SSFPQL cannot be explained by this.

However, for a realistic comparison between theory and data, the hydrogen contribution to the FIDA tomography must be added. It is already plotted in figures 8 and 9, and we will discuss it in details in the next section.

4.3 The hydrogen contribution

The TORIC/SSFPQL code gives the hydrogen distribution function directly as output, while TRANSP yields only parallel and perpendicular temperatures. The respective profiles are shown in fig. 11 for the considered time point (4.6 s). For comparison, the parallel and perpendicular temperatures of TORIC/SSFPQL are shown with a dotted line. They are defined via the flux-surface average of the average energies of the distribution function: $T_\parallel = 2\langle E_\parallel \rangle$ and $T_\perp = \langle E_\perp \rangle$. The ICRH accelerates hydrogen mainly in the core region between $\rho_{\mathrm{tor}} = 0.0 - 0.4$. Here, the predicted $T_\perp$ from TORIC/SSFPQL is slightly higher (factor ≈ 1.25) than from TRANSP and also $T_\parallel$ is higher in TORIC/SSFPQL.

A possible explanation for this deviation could be that the considered time point (4.6 s) is too close to the ICRH switch-on at 4.5 s, such that a steady state is not reached yet (as it is assumed by TORIC/SSFPQL). We have investigated this in the same way as for the deuterium distribution function above, by calculating a dedicated TRANSP run, where we keep the kinetic profiles and the heating power constant after 4.6 s. The temporal evolution of the hydrogen temperatures, as result of this TRANSP run, are shown in fig. 11c with a dashed line in comparison to a realistic TRANSP run (full line). The considered time point lies well after the strong rise of the temperatures following the ICRH-onset at 4.5 s. However, from the dashed curve it can be concluded, that a full steady state is not yet reached entirely for hydrogen. Instead, $T_\perp$ rises further and reaches its steady-state level asymptotically. The reason why hydrogen is not yet close to a steady state (while deuterium is) can be given by the much higher energies, which take more time to be reached. The TRANSP steady state solution (evaluated at 4.95 s) is then even higher than SSFPQL (see fig. 11a). This is in line with the fact that TORIC/SSFPQL predicts a lower hydrogen heating power than TRANSP (1.35 MW vs. 1.49 MW, compare also fig. 17) in favor of stronger D heating.

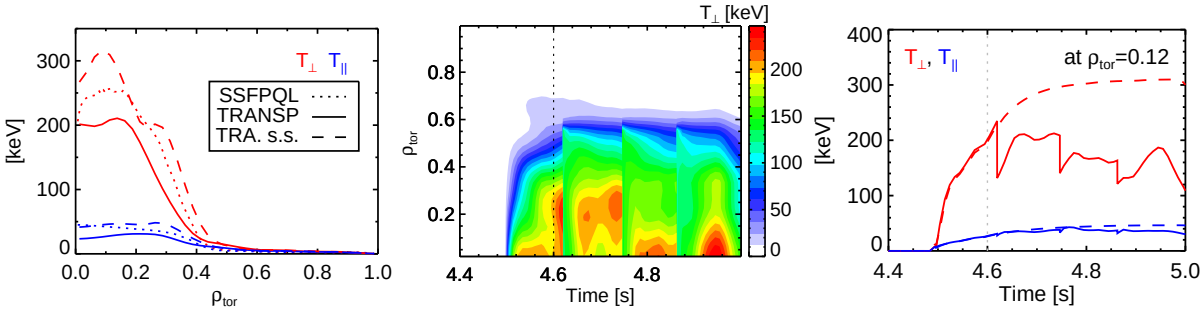

(a) **(b)** **(c)**

Figure 11: Perpendicular and parallel hydrogen temperatures $T_\perp$ and $T_\parallel$ (flux surface average). **(a)** Profiles at 4.6 s. In addition, the steady state solution of TRANSP is shown (TRA. s.s.). **(b)** Contour plot of the temporal evolution of the $T_\perp$-profile (TRANSP) **(c)** Time traces at $\rho_{\mathrm{tor}} = 0.12$ (TRANSP). The dashed lines correspond to a simulation without sawtooth modeling and with constant kinetic profiles and heating power after 4.6 s.

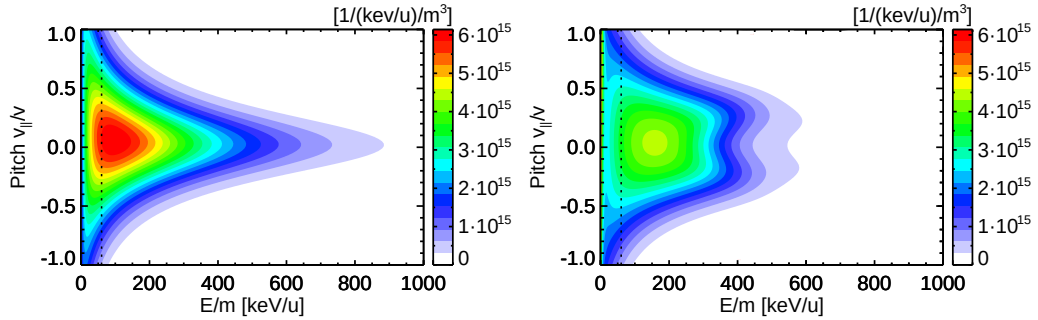

(a) TRANSP (Bi-Maxwellian) **(b)** TORIC/SSFPQL

Figure 12: Hydrogen distribution functions. The FIDA tomography observes only the small region on the left of the dashed line.

The values of $T_\parallel$ and $T_\perp$ from TRANSP can be used to model the H distribution function with a bi-Maxwell-Boltzmann distribution. For the considered measurement position ($\rho_{\mathrm{tor}} = 0.12$ on the low field side), this is shown in fig. 12 in comparison to the TORIC/SSFPQL H distribution function. The TORIC/SSFPQL solution includes a correction of the quasi-linear RF operator for particle trapping, which leads to resonance localization and the characteristic rabbit-ear shape. The velocity space region which is observed by the FIDA tomography (< 60 keV/u) is indicated with a dashed line. Due to high $T_\perp$, a large fraction of hydrogen is located at much higher energies, which are not observable by the FIDA diagnostic, because the charge exchange cross-sections are small for large energies. The part which is observable, shows a rather broad pitch distribution. Hence, for high hydrogen temperatures, the hydrogen contribution to the FIDA tomography can be considered as a smoothly spread background, but well localized peaks or high energy tails in the tomography cannot be explained by hydrogen. The H contribution gets weaker with increasing H temperatures, because the phase space density is then lowered in the FIDA energy region (< 60 keV/u).

The sum of hydrogen and deuterium is shown in the energy and pitch profiles (figures 8 and 9) with full lines. For TRANSP, the hydrogen contribution is stronger than for TORIC/SSFPQL, because of its lower H temperatures. Nevertheless, hydrogen cannot explain the difference between TRANSP and the tomography, which suggests that TRANSP underestimates the D acceleration by second harmonic ICRH in the observed energy range.

In this section, we have demonstrated that the FIDA tomography is able to detect an ICRH-induced high energy tail in the center-most measurement position. TRANSP predicts a weaker and TORIC/SSFPQL a stronger tail. In the next section, we will investigate the other, more-outward radial positions, for which FIDA tomographies can be calculated, and study the radial dependence.

5 Radial dependence

We have calculated FIDA tomographies at six different radial positions (all on the low field side). The lines of sight, which have been grouped for each position, are indicated in fig. 3 by boxes. All radial positions have at least three FIDA views, and half of them (like the center-most one, which we have discussed in the previous section) have an additional fourth FIDA view. Contour plots of the reconstructed fast-ion velocity distribution are shown in fig. 13 for all positions, and the NBI-only and NBI+ICRH phase.

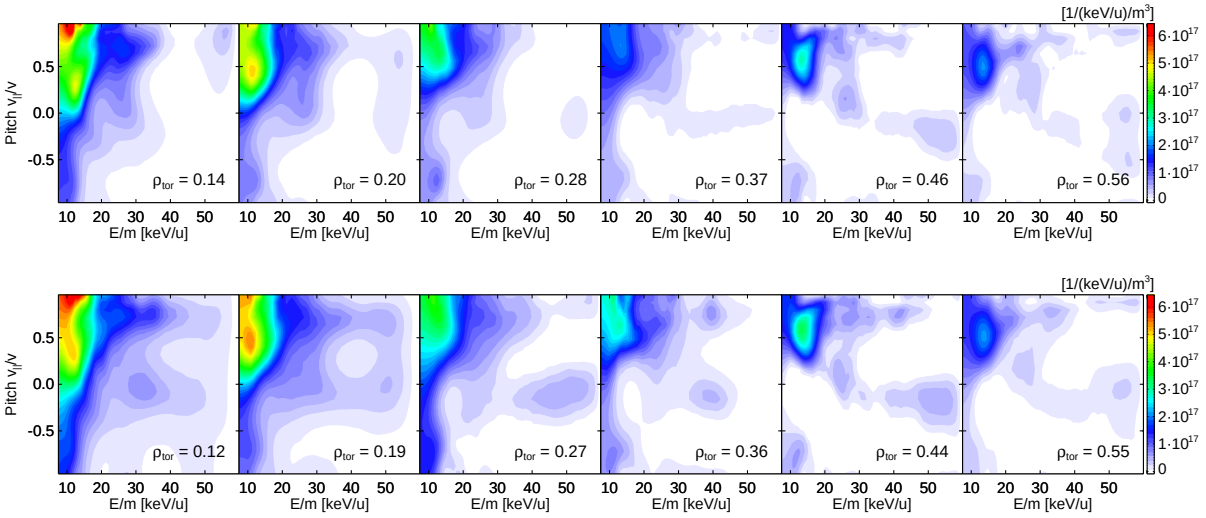

Figure 13: FIDA tomographies at different radial positions. Top: 4.48s (NBI only), bottom: 4.60s (NBI+ICRH)

In the NBI only phase, all radial positions show mainly fast ions below the injection energy (30 keV/u), as it is expected. Also, the reconstructed distribution is aligned around $\xi \approx 0.6$, which is very well in agreement with the geometry of NBI Q3. Moreover, the basic shape of the distribution function is in agreement with the theoretical prediction, plotted in figure 14. Above the injection energy some randomly distributed small peaks are visible which can be identified as artifacts. Most artifacts are seen in the two outer-most radial positions. This can be explained because these channels have a lower signal-to-noise

ratio, since the fast-ion density is much lower in those channels. In addition, most of the artifacts appear towards high energies $E/m > 50$ keV/u. This might be explainable by the fact that the absolute values of the FIDA weight functions (which yield how many photons are emitted by a given fast ion [29]) decreases towards high energies, because the charge exchange cross-sections go down. Hence, a small perturbation in the FIDA signal gets translated into more fast ions in the tomography towards higher energies. The area below 50 keV/u is much less affected by artifacts, and is well suited for the physics analysis.

In the NBI+ICRH phase, high energy tails above the injection energy are clearly seen in the two center-most positions. The tails get weaker in the two intermediate radial positions ($\rho_{\mathrm{tor}} = 0.27$ and $\rho_{\mathrm{tor}} = 0.36$). In the two outermost positions ($\rho_{\mathrm{tor}} = 0.46$ and $\rho_{\mathrm{tor}} = 0.55$), only weak structures are left, which cannot be clearly distinguished from artifacts anymore.

The contour plots of the calculated deuterium distribution by TRANSP and TORIC-SSFPQL are shown in figures 14 and 15 for the NBI-only and NBI+ICRH phase, respectively. To compare simulation results and FIDA tomography quantitatively, we compute radial profiles by integrating in the velocity space over an energy region of interest I and over all pitches: $\int_I \int_{-1}^{+1} F(\frac{E}{m}, \xi) \mathrm{d}\frac{E}{m} \mathrm{d}\xi$. We define two such regions of interest: $I_1 = [20, 35]$ keV/u and $I_2 = [35, 50]$ keV/u. The first interval corresponds to the highest energy component of the beam ions, such that we can compare radial profiles of the full-energy beam ion density. The upper boundary of the interval has been chosen such that we integrate over the area, where the step at the injection energy is typically smeared out in the FIDA tomography (comp. fig. 8). The second interval $I_2 = [35, 50]$ keV/u is aligned then towards high energies and measures the fast-ion density in high energy tails, well above the NBI injection energy. The upper boundary is set to 50 keV/u to avoid picking up the aforementioned artifacts which are visible in the tomography above this boundary.

The resulting profiles for both the NBI-only and NBI+ICRH phases are shown in fig. 16. For the NBI-only phase, excellent agreement is found between the beam-ion density (I_1) of TRANSP and the FIDA tomography. The SSFPQL solution appears to be more strongly peaked, such that the inner-most point is higher. The high energy region (I_2) shows a FIDA tomography close to zero, as it is expected. This shows that this energy region is indeed mostly free of tomography artifacts, such that it is well suited for studying high energy tails.

In the NBI+ICRH phase, again good agreement is found between TRANSP and the FIDA tomography for the beam ions in the interval $I_1 = [20, 35]$ keV/u. The hydrogen contribution is very small compared to the beam ions and does not change the picture significantly. As in the NBI-only phase, the TORIC/SSFPQL prediction shows good agreement in the outer plasma, but appears higher and more strongly peaked towards the plasma center. In the NBI+ICRH phase, this deviation is even higher than in the NBI-only phase.

In the high energy region I_2, the FIDA tomography shows a peaked profile. This is within expectations, since the ICRH resonance layer is situated close to the magnetic axis. Also, this proves that passive FIDA light (from the plasma edge) does not contribute significantly to the signal, as it would be visible in all lines of sight. It can furthermore

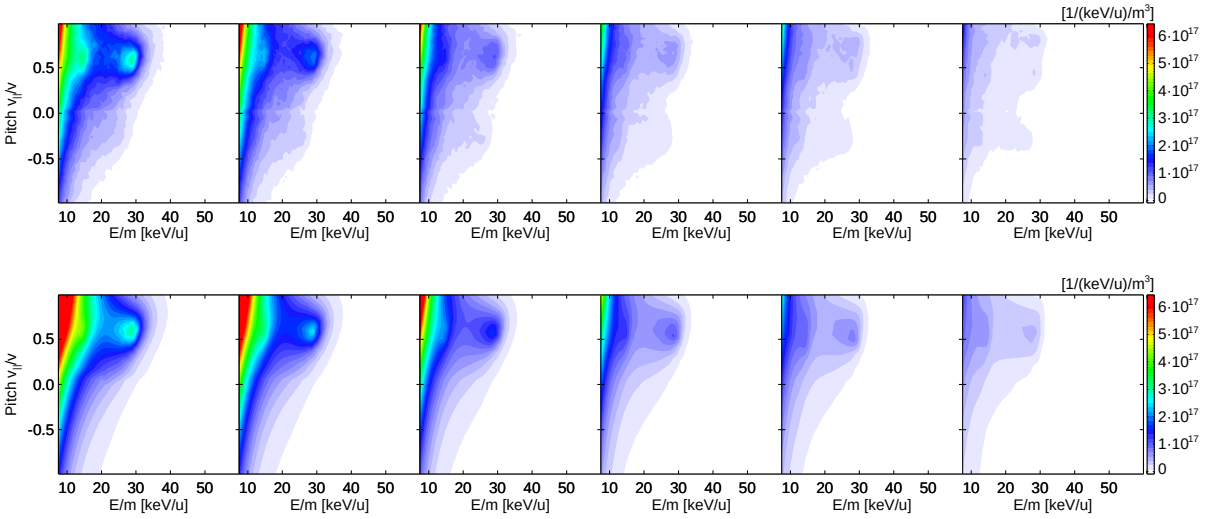

Figure 14: Calculated D fast-ion distribution from TRANSP (top) and TORIC/SSFPQL (bottom) in the NBI-only phase (4.48s).

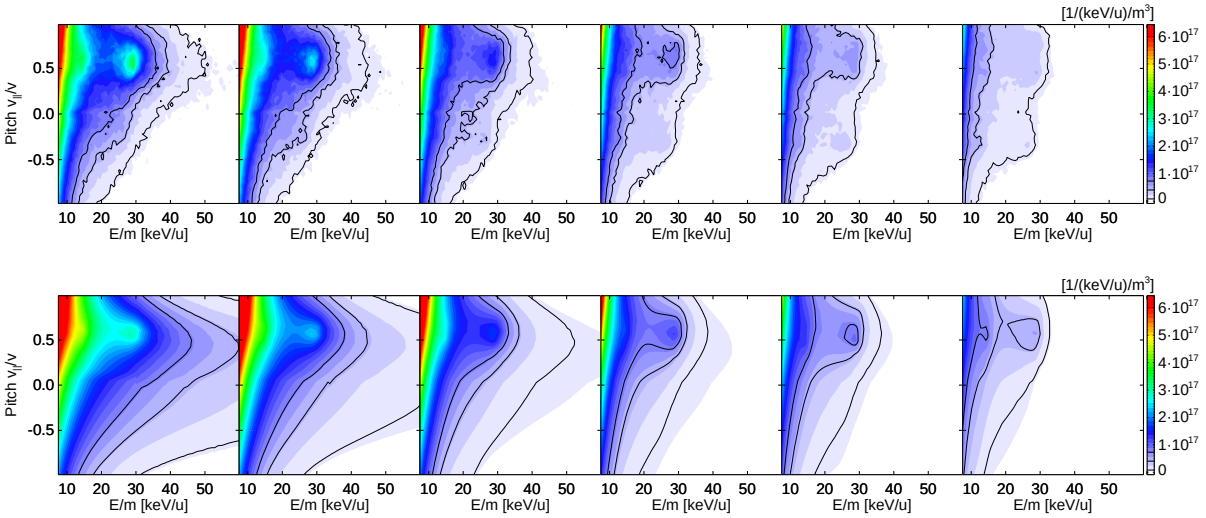

Figure 15: Calculated H+D fast-ion distribution from TRANSP (top) and TORIC/SSFPQL (bottom) in the NBI+ICRH phase (4.60s). The color scale refers to the sum of hydrogen and deuterium. For comparison, the first, third and fifth contour lines are drawn in black for the sole deuterium distribution.

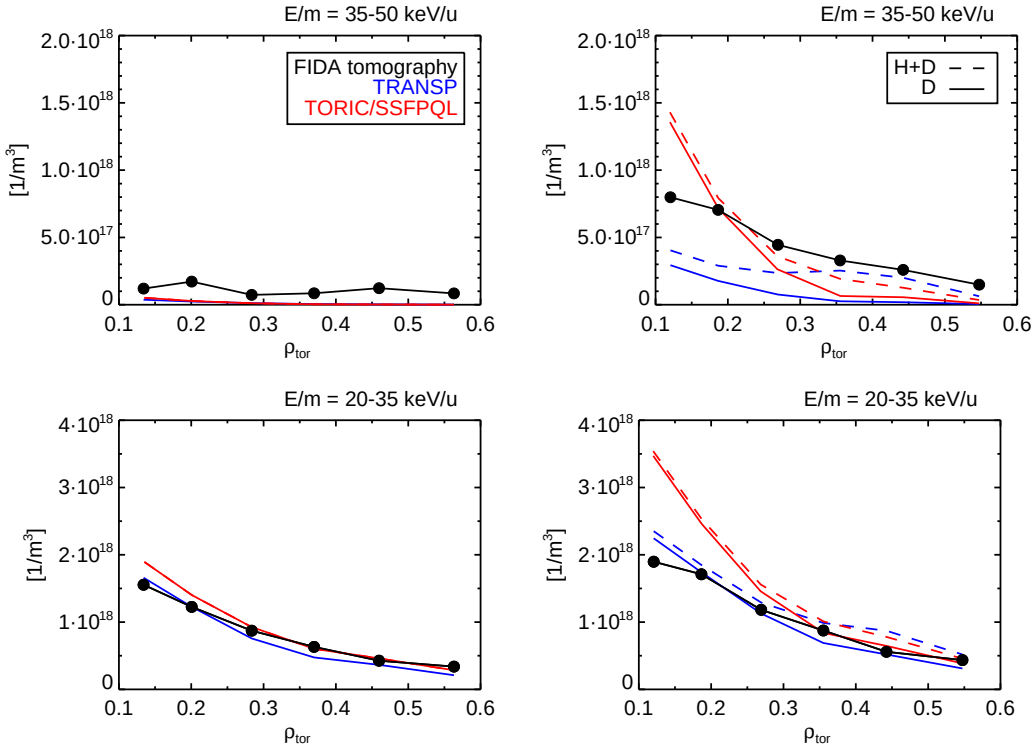

(a) 4.48s (NBI-only) **(b)** 4.60s (NBI+ICRH)

Figure 16: Radial fast-ion density profiles in two different E/m ranges (top and bottom)

be seen, that the TRANSP prediction is lower than the measured value for the three central positions, also if the hydrogen contribution is taken into account (plotted with the dashed line). This is in line with the results, which we have found for the inner-most radial position in the previous section. For $\rho_{\mathrm{tor}} > 0.3$ good agreement is found between the FIDA tomography and the H+D estimate from TRANSP.

The TORIC/SSFPQL result shows a different radial behavior: In the plasma center, the high energy tail is much stronger than in the FIDA tomography, as discussed already in the previous section. Further outwards ($\rho_{\mathrm{tor}} \gtrsim 0.35$) it is lower and goes faster to zero. To some extent this might be explainable by the zero-orbit-width approximation which is assumed in TORIC/SSFPQL. Taking into account the orbit widths should lead to a broadening of the profile, which could improve the agreement with the experimental data, in particular because the differential volume $\mathrm{d}V/\mathrm{d}\rho_{\mathrm{tor}}$ is small close to the magnetic axis and increases with ρ_{tor}. Such an upgrade has already been implemented in the CQL3D code, which resulted an improved agreement with experimental FIDA data [44, 45].

A possible reason for the underprediction from TRANSP could be the fact that TRANSP distinguishes between thermal and "fast" deuterium (i.e. beam ions). Figure 17 shows the distribution of absorbed ICRH power among the different plasma species. Absorption by electrons is weak for both codes and does not play an important role. In general, TRANSP predicts that less ICRH power is absorbed by deuterium (2^{nd} harmonic) than TORIC/SSFPQL. In addition, TRANSP separates the 2^{nd} harmonic absorption for thermal and beam ions. The latter is calculated with the Monte Carlo Kick operator

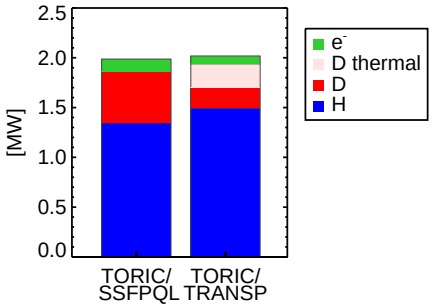

Figure 17: Calculated ICRH absorption power for the different particle species. The TRANSP code separates between thermal and fast deuterium ion, while SSFPQL treats them uniformly and consistently.

and appears in the beam-ion distribution function, which we use for comparison with the FIDA tomography. Due to high T_i, 2nd harmonic absorption is also quite efficient for the thermal D population. In fact, TRANSP predicts slightly more power absorption by thermal deuterium than by fast deuterium. However, this thermal contribution is missing in the comparison with the FIDA tomography. TRANSP uses the power for the power balance evaluation, but the thermal D distribution is still considered to be "thermal", i.e. Maxwellian. Deviations from a Maxwellian shape (e.g. high energy tails) are neglected. As mentioned previously, we add the thermal deuterium distribution function to the beam-ion distribution function for the comparison with the FIDA tomography. Nevertheless, high energy tails originating from the acceleration of thermal D are not included in this approach, as they are not given in the TRANSP output. This could explain, why the TRANSP prediction is lower than the FIDA tomography.

It is interesting to note that the simulated hydrogen contribution has its maximum in the region around $\rho_{tor} \approx 0.35-0.40$, both in the TRANSP and TORIC/SSFPQL results. Since we have assumed a constant hydrogen concentration of 5% in the whole plasma and the electron density is rather flat in the core region, this can only be explained by the hydrogen temperature profiles (fig. 11): At $\rho_{tor} \approx 0.35-0.40$, the perpendicular hydrogen temperature falls down to values in the range of $T_\perp \approx 50$ keV. Hence, a much larger fraction of the H distribution function lies in the energy region observed by the FIDA tomography. Further outward, the hydrogen contribution vanishes as H temperatures approach thermal levels, and further inwards the H temperatures are too high, such that only a small fraction of their velocity distribution intersects with the FIDA tomography energy range.

6 Comparison with other fast-ion measurements

In this section, we compare how the effect of 2nd harmonic ICRH on the beam ion distribution is measured by other fast-ion diagnostics.

6.1 Neutral particle analyzer

Fig. 18 shows measurements of the recently installed active neutral particle analyzer (aNPA) [46] for the same time points as above. The NPA compact solid-state detector

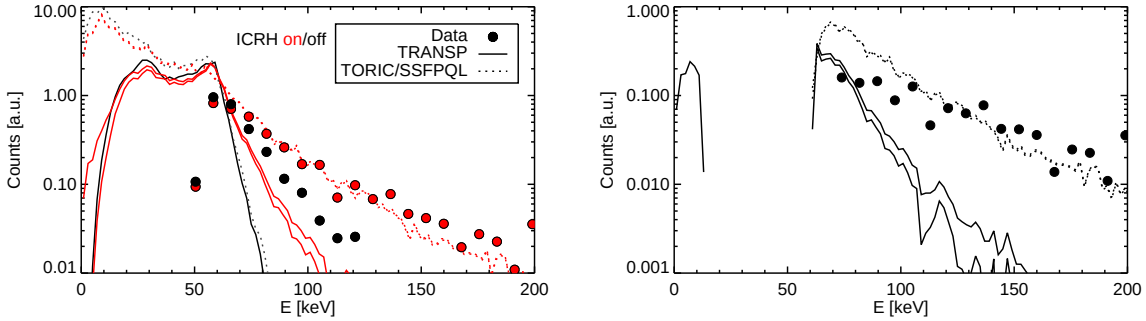

(a) 4.48s (NBI-only, black) and 4.60s (NBI+ICRH, red)

(b) Difference between both time points

Figure 18: Measurements from the active neutral particle analyzer in comparison with theoretical prediction. For the NBI+ICRH phase, the calculated D fluxes and the H+D fluxes are both shown. For TRANSP, the H+D fluxes are identified by the higher line. For TORIC/SSFPQL, the D fluxes are so high that the H+D fluxes are almost identical.

measures escaping neutrals originating from re-neutralization of fast ions by charge exchange. In contrast to passive NPAs, the active NPA is aligned at an NBI beam (source Q3) and utilizes its injected neutral atoms as donor neutrals for the charge-exchange reactions. The measurement is hence localized in a region in the plasma center, with an additional contribution from the plasma edge (where neutral densities are high, too). The detector measures particles with pitches $\xi \approx 0.6$ (due to the line-of-sight geometry) and is mainly sensitive to energies above 40 keV. Lower energies are blocked by a thin aluminum foil. During discharges an increasing noise level - likely due to heating up of the detector - can obscure also particles with higher energies, in the presented case up to 60 keV. One of the major advantages of the NPA over the FIDA diagnostic is, that it can measure signal levels over several orders of magnitude. This allows to study higher energy ranges (here: up to 200 keV) which are not accessible for FIDA (here: < 120 keV).

In comparison to the measurement, we show the theoretical prediction from TRANSP and TORIC/SSFPQL both for H and D. They are calculated by forward-modeling the distribution functions with FIDASIM, which is equipped with a synthetic NPA diagnostic. The aNPA is not absolutely calibrated, such that the forward-modeled spectra needs to be scaled to allow a shape comparison. For this purpose we have matched absolute values of the NBI-only simulations to the experiment at around 65 keV and used the same scale factor for the NBI+ICRH simulations.

In the NBI-only phase, both codes predict a much steeper fall-off above the injection energy than it is measured. This feature is regularly observed with the active neutral particle analyzer, and the reason behind this is not completely understood yet. All obvious diagnostic artifacts could be excluded to cause this measurement [46].

In the NBI+ICRH phase, an increase of the measured high-energy tail is observed. Forward-modeling suggests that the hydrogen contribution to the NPA flux is low, such that we can interpret this as a confirmation of deuterium acceleration due to 2^{nd} harmonic ICRF absorption. The measured high energy tail is flatter (and thus stronger) than the prediction by TRANSP/NUBEAM, which is in agreement with the previous findings with the FIDA tomography. The agreement with TORIC/SSFPQL is remarkably good.

This could be interpreted by the larger measurement volume of the NPA, i.e. that the core region, where TORIC/SSFPQL predicts a too strong high energy tail, is balanced by outer regions, where the prediction is e.g. lower than the FIDA tomography (see the top row of fig. 16b). However, the fact that measurement and simulation do not agree in the NBI-only reference case, makes it difficult to draw strong conclusions. If one compares, for example, the difference between the NBI-only phase and NBI+ICRH phase, then neither of the codes shows a good agreement with the experimental observation.

6.2 Neutron rates

Another diagnostic principle, which is very sensitive to fast deuterium ions, is the measurement of neutrons resulting from the D-D fusion reaction. An advantage of this method is that no contribution from hydrogen has to be considered, as hydrogen does not produce neutrons (neither in H+H nor in H+D reactions).

Fig. 19 shows the raw data of the NES detector (a recently installed neutron spectrometer [6] based on the liquid scintillator BC501A) and a comparison of the NES signal to theoretical prediction by TRANSP and TORIC/SSFPQL. The latter calculates only the steady state solution, which is shown with dots for the two time-points. TRANSP calculates the full temporal evolution of the neutron rate. To compare measurement and theory, the calibrated measurements were scaled to the TRANSP prediction at 4.4s. It should be noted that the codes calculate the volume integrated neutron rate, while the diagnostic measures a line integrated neutron rate (along its line of sight). To take this into account, we have used a synthetic NES diagnostic, which is able to forward model synthetic signals (shown with blue symbols) from the TRANSP output.

Both theoretical codes predict very similar neutron rates in the NBI-only phase. It should be noted that the relatively high plasma rotation plays here a crucial role for the calculation of the neutron rate. In TORIC-SSFPQL simulations with zero toroidal plasma rotation the neutron rate is $\approx 20\,\%$ higher. This can be explained, because the plasma rotates in the same direction as the beam is injecting, which reduces the injection energy in the plasma frame (e.g. in the NBI-only phase from 58.4 keV to 51.6 keV in the plasma center). Since the neutron rate is very sensitive to the high-energy part of the distribution function, this reduces the neutron rate significantly. For the comparison with NPA and FIDA diagnostics, the plasma rotation has a much weaker effect, because they measure in the lab frame and therefore see e.g. the beam peaks still at the nominal NBI injection energy and not at the reduced energy in the plasma frame.

With respect to the NBI-only phase, TRANSP predicts a neutron enhancement in the NBI+ICRH phase at 4.6s of a factor of ≈ 1.7, which is slightly smaller than the measured factor (≈ 1.8) but in reasonable agreement. A more realistic calculation including diagnostic effects (based on forward-modeling) is shown with blue symbols and yields the same predicted enhancement of ≈ 1.7. In contrast, TORIC/SSFPQL predicts a much stronger increase (factor ≈ 4.3), which is not in line with the measurement. In the analysis of the FIDA tomography, we have seen that TORIC/SSFPQL predicts too strongly peaked fast-ion density profiles with very strong high-energy tails in the plasma center (i.e. D ions are accelerated to much higher energies than in TRANSP). This leads to the strong neutron-rate overprediction.

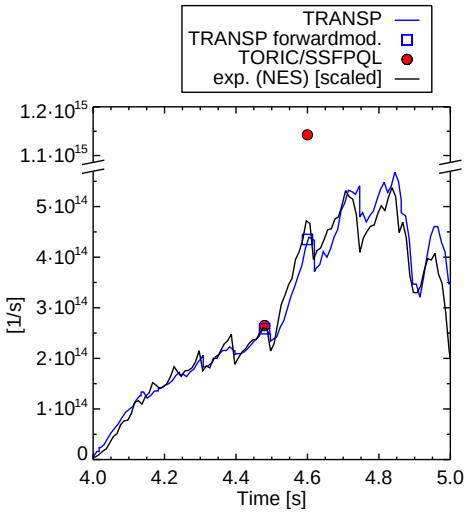

Figure 19: Neutron measurements: Comparison of the NES signal with theoretical predictions. The experimental signal is scaled to match the TRANSP prediction at 4.48 s (due to missing absolute calibration).

Furthermore, we have concluded from the FIDA tomography that TRANSP has a weaker fast-deuterium high energy tail at the two inner-most FIDA measurement positions. In the neutron rate, this underestimation by TRANSP is only weakly visible, while the overall evolution of the neutron rate fits quite reasonably with experimental data. This can be interpreted by the fact that the neutron rate measurement integrates both over real and velocity space, and thus is not very sensitive for such small and localized deviations. In addition, the neutron rate increase is also caused by other effects such as the increasing electron density (see fig. 2) and the fast-ion density increase in other regions of the velocity space, where good agreement between TRANSP and the FIDA tomography is found (e.g. the lower row of fig. 16).

It should be noted that the neutron rate is quite sensitive to Z_{eff} (it is reduced by increasing Z_{eff}). This is problematic for the analysis of neutron rates, because the temporal evolution of Z_{eff} cannot be measured reliably. In both codes, we have assumed that it is time-invariant. It might be that the impurity content increases after switching on ICRH due to sputtering induced by the antenna currents and fields. This is often observed in ASDEX Upgrade experiments. In addition, no ECRH is used in this discharge to counteract a possible impurity accumulation. This has to be kept in mind when drawing quantitative conclusions from the neutron rate.

7 Summary and Conclusion

In this paper, we investigate the acceleration of fast deuterium ions by 2$^{\text{nd}}$ harmonic ion cyclotron resonance heating and we demonstrate that the FIDA tomography technique is a valuable tool to assess this physical question. In our analysis, a phase within a discharge with NBI only is compared to a phase with NBI+ICRH. In this ICRH scenario, hydrogen is resonant at the first harmonic. Since a residual hydrogen concentration of about 5% is typically present at ASDEX Upgrade, it absorbs ICRH power in competition

with deuterium and needs to be considered in the data analysis. We show that the FIDA tomography can be interpreted as sum of the deuterium and hydrogen distribution function, if it is written as function of E/m.

In the NBI+ICRH phase, the tomographic reconstructions in the plasma center yield two distinct high-energy tails above the NBI energy, which are not present in the NBI-only phase. Theoretical considerations suggest that the hydrogen distribution function is much broader in the considered energy range. Hence, hydrogen can contribute to the total integral over the peaks, but the well-defined shape of the peaks suggest that they originate mainly from deuterium.

In total, we calculate tomographic reconstructions at six radial positions distributed from the plasma center to the low field side periphery. This is in particular the first time that a radial profile of the fast-ion velocity distribution is reconstructed from FIDA measurements. The high-energy tails vanish in the outer-most radial positions, which is in agreement with the expected ICRH deposition position.

A comparison to theory is carried out with predictions from the TRANSP/TORIC and TORIC/SSFPQL codes. In the NBI-only phase good agreement can be concluded between both codes and experimental observations. In the ICRH phase, TORIC/SSFPQL predicts a too strongly peaked fast-ion profile, which could be caused by missing orbit effects in the code. This results also in a strong overprediction of the neutron rate. In contrast, TRANSP/TORIC predicts a slightly weaker neutron rate enhancement than measured, which can be however still be considered as reasonable agreement. The FIDA tomography allows a more detailed comparison (i.e. spatially and velocity-space resolved). This reveals that the high-energy tails (above the NBI energy) are underestimated by TRANSP/TORIC in the plasma center. This trend is also supported by the (core-localized) active NPA measurements. For lower energies (around and below the NBI energy) good agreement between FIDA and TRANSP/TORIC is found throughout.

In conclusion, the TRANSP/TORIC code package (with the TORIC kick operator in NUBEAM) tends to underestimate the effect of 2^{nd} harmonic ICRH in comparison to experimental data. While non-localized and velocity-space integrated measurements like the neutron rate still are in reasonable agreement, the good resolution both in real and velocity space of the FIDA tomography reveals that the predicted ICRH-induced high energy tails are too weak in the plasma center. This leaves room for improvement of the theoretical model.

TORIC/SSFPQL predicts a stronger 2^{nd} harmonic ICRH than TRANSP/NUBEAM, but the results are also not in good agreement with experimental data. The radial deuterium fast-ion density profiles are peaked too strongly and the predicted neutron rate increase is too high by a factor of ≈ 2.4. Possible explanations for this disagreement are the missing orbit physics. Each radial cell in the SSFPQL Fokker-Planck solver is independent of each other, which means that radial transport is neglected, and the ion orbits are assumed to move on flux surfaces (zero orbit width approximation). Furthermore, particle trapping is only considered in the quasi-linear RF operator. The orbits of ICRH accelerated ions can however have very large excursions from their initial flux surface, because drift velocities are high due to high ion energies, while the parallel velocity component (i.e. the pitch $v_{\parallel}/v$) is rather low. In addition, a large fraction of ICRH ions is expected to be on trapped or stagnation orbits, which have a even larger orbit

width than passing orbits. Furthermore, collisional radial transport is proportional to the orbit widths. An inclusion of these effects into the TORIC/SSFPQL model is subject of ongoing work. It could lead to a broadening of the fast-ion profiles and thus substantially improve the agreement with experimental data.

Acknowledgments

We would like to thank M. Brambilla for fruitful discussions. This work has been carried out within the framework of the EUROfusion Consortium and has received funding from the Euratom research and training programme 2014-2018 under grant agreement No 633053. The views and opinions expressed herein do not necessarily reflect those of the European Commission.

References

[1] D. W. Swain and R. H. Goulding. ITER ion cyclotron system: Overview and plans. *Fusion Engineering and Design*, 82(5):603–609, 2007.

[2] W. Heidbrink and G. Sadler. The behaviour of fast ions in tokamak experiments. *Nuclear Fusion*, 34(4):535, 1994.

[3] W. W. Heidbrink, Y. Luo, K. H. Burrell, R. W. Harvey, R. I. Pinsker, and E. Ruskov. Measurements of fast-ion acceleration at cyclotron harmonics using Balmer-alpha spectroscopy. *Plasma Physics and Controlled Fusion*, 49(9):1457, 2007.

[4] J. Hosea, S. Bernabei, P. Colestock, S. Davis, P. Efthimion, R. Goldston, D. Hwang, S. Medley, D. Mueller, J. Strachan, et al. Fast-wave heating of two-ion plasmas in the Princeton Large Torus through minority-cyclotron-resonance damping. *Physical Review Letters*, 43(24):1802, 1979.

[5] C. Hellesen, M. G. Johnson, E. A. Sundén, S. Conroy, G. Ericsson, E. Ronchi, H. Sjöstrand, M. Weiszflog, G. Gorini, M. Tardocchi, T. Johnson, V. Kiptily, S. Pinches, S. Sharapov, and J.-E. Contributors. Neutron emission generated by fast deuterons accelerated with ion cyclotron heating at JET. *Nuclear Fusion*, 50(2):022001, 2010.

[6] G. Tardini, A. Zimbal, B. Esposito, F. Gagnon-Moisan, D. Marocco, R. Neu, H. Schuhmacher, and the ASDEX Upgrade Team. First neutron spectrometry measurements in the ASDEX Upgrade tokamak. *Journal of Instrumentation*, 7(03):C03004, 2012.

[7] D. Darrow, C.-S. Chang, S. Zweben, R. Budny, H. Herrmann, E. Jaeger, R. Majeski, M. Murakami, C. Phillips, J. Rogers, G. Schilling, J. Stevens, and J. Wilson. ICRF-induced DD fusion product losses in TFTR. *Nuclear Fusion*, 36(1):1, 1996.

[8] M. Garcia-Munoz, H.-U. Fahrbach, S. Günter, V. Igochine, M. J. Mantsinen, M. Maraschek, P. Martin, P. Piovesan, K. Sassenberg, and H. Zohm. Fast-ion Losses due to High-frequency MHD Perturbations in the ASDEX Upgrade Tokamak. *Physical Review Letters*, 100(5):055005, 2008.

[9] V. Kiptily, F. Cecil, O. Jarvis, M. Mantsinen, S. Sharapov, L. Bertalot, S. Conroy, L. Ingesson, T. Johnson, K. Lawson, S. Popovichev, and contributors to the EFDA-JET Workprogramme. γ-ray diagnostics of energetic ions in JET. *Nuclear Fusion*, 42(8):999, 2002.

[10] V. Kiptily, J. Adams, L. Bertalot, A. Murari, S. Sharapov, V. Yavorskij, B. Alper, R. Barnsley, P. de Vries, C. Gowers, L.-G. Eriksson, P. Lomas, M. Mantsinen, A. Meigs, J.-M. Noterdaeme, F. Orsitto, and J. E. contributors. Gamma-ray imaging of D and 4 He ions accelerated by ion-cyclotron-resonance heating in JET plasmas. *Nuclear Fusion*, 45(5):L21, 2005.

[11] H. Bindslev, J. Hoekzema, J. Egedal, J. Fessey, T. Hughes, and J. Machuzak. Fast-ion velocity distributions in JET measured by collective Thomson scattering. *Physical review letters*, 83(16):3206, 1999.

[12] D. Liu, W. W. Heidbrink, M. Podestà, R. E. Bell, E. D. Fredrickson, S. S. Medley, R. W. Harvey, and E. Ruskov. Profiles of fast ions that are accelerated by high harmonic fast waves in the National Spherical Torus Experiment. *Plasma Physics and Controlled Fusion*, 52(2):025006, 2010.

[13] B. Geiger, R. Dux, R. M. McDermott, S. Potzel, M. Reich, F. Ryter, M. Weiland, D. Wünderlich, ASDEX Upgrade Team, and M. Garcia-Munoz. Multi-view fast-ion D-alpha spectroscopy diagnostic at ASDEX Upgrade. *Review of Scientific Instruments*, 84(11):–, 2013.

[14] M. Weiland, B. Geiger, A. S. Jacobsen, M. Reich, M. Salewski, T. Odstrčil, and the ASDEX Upgrade Team. Enhancement of the FIDA diagnostic at ASDEX Upgrade for velocity space tomography. *Plasma Physics and Controlled Fusion*, 58(2):025012, 2016.

[15] M. Salewski, B. Geiger, S. Nielsen, H. Bindslev, M. García-Muñoz, W. Heidbrink, S. Korsholm, F. Leipold, F. Meo, P. Michelsen, D. Moseev, M. Stejner, G. Tardini, and the ASDEX Upgrade team. Tomography of fast-ion velocity-space distributions from synthetic CTS and FIDA measurements. *Nuclear Fusion*, 52(10):103008, 2012.

[16] M. Salewski, B. Geiger, A. Jacobsen, M. García-Muñoz, W. Heidbrink, S. Korsholm, F. Leipold, J. Madsen, D. Moseev, S. Nielsen, J. Rasmussen, M. Stejner, G. Tardini, M. Weiland, and the ASDEX Upgrade Team. Measurement of a 2D fast-ion velocity distribution function by tomographic inversion of fast-ion D-alpha spectra. *Nuclear Fusion*, 54(2):023005, 2014.

[17] M. Brambilla. Quasi-linear ion distribution function during ion cyclotron heating in tokamaks. *Nuclear fusion*, 34(8):1121, 1994.

[18] Y. Feng, B. Wolle, and K. Hübner. New, simplified technique for calculating particle source rates due to neutral beam injection into tokamaks. *Computer physics communications*, 88(2):161–172, 1995.

[19] M. Brambilla. Numerical simulation of ion cyclotron waves in tokamak plasmas. *Plasma Physics and Controlled Fusion*, 41(1):1, 1999.

[20] M. Brambilla and R. Bilato. Advances in numerical simulations of ion cyclotron heating of non-Maxwellian plasmas. *Nuclear Fusion*, 49(8):085004, 2009.

[21] R. Bilato, M. Brambilla, O. Maj, L. Horton, C. Maggi, and J. Stober. Simulations of combined neutral beam injection and ion cyclotron heating with the TORIC-SSFPQL package. *Nuclear Fusion*, 51(10):103034, 2011.

[22] R. Hawryluk and et al. An Empirical Approach to Tokamak Transport. *in Physics of Plasmas Close to Thermonuclear Conditions*, 1:19–46, 1980.

[23] R. J. Goldston, D. McCune, H. Towner, S. Davis, R. Hawryluk, and G. Schmidt. New techniques for calculating heat and particle source rates due to neutral beam injection in axisymmetric tokamaks. *Journal of computational physics*, 43(1):61–78, 1981.

[24] A. Pankin, D. McCune, R. Andre, G. Bateman, and A. Kritz. The tokamak Monte Carlo fast ion module NUBEAM in the National Transport Code Collaboration library. *Computer Physics Communications*, 159(3):157 – 184, 2004.

[25] N. Bertelli, E. Valeo, D. Green, M. Gorelenkova, C. Phillips, M. Podestà, J. Lee, J. Wright, and E. Jaeger. Full-wave simulations of ICRF heating regimes in toroidal plasma with non-Maxwellian distribution functions. *Nuclear Fusion*, 57(5):056035, 2017.

[26] R. Bartiromo, G. Bracco, M. Brusati, G. Grosso, S. Mantovani, B. Tilia, and V. Zanza. Design and calibration of the JET neutral particle analyzer. *Review of Scientific Instruments*, 58(5), 1987.

[27] W. Heidbrink, D. Liu, Y. Luo, E. Ruskov, and B. Geiger. A code that simulates fast-ion D-alpha and neutral particle measurements. *Comm. Comp. Physics*, 10:716–741, 2011.

[28] B. Geiger. *Fast-ion transport studies using FIDA spectroscopy at the ASDEX Upgrade tokamak*. Phd thesis, LMU München, 2013. also IPP report 10/46.

[29] M. Salewski, B. Geiger, D. Moseev, W. W. Heidbrink, A. S. Jacobsen, S. B. Korsholm, F. Leipold, J. Madsen, S. K. Nielsen, J. Rasmussen, M. Stejner, M. Weiland, and ASDEX Upgrade Team. On velocity-space sensitivity of fast-ion D-alpha spectroscopy. *Plasma Physics and Controlled Fusion*, 56(10):105005, 2014.

[30] B. Geiger, M. Weiland, A. Jacobsen, D. Rittich, R. Dux, R. Fischer, C. Hopf, M. Maraschek, R. McDermott, S. Nielsen, T. Odstrcil, M. Reich, F. Ryter, M. Salewski, P. Schneider, and G. Tardini. Fast-ion transport and neutral beam current drive in ASDEX Upgrade. *Nuclear Fusion*, 55(8):083001, 2015.

[31] M. Salewski, B. Geiger, A. Jacobsen, P. Hansen, W. Heidbrink, S. Korsholm, F. Leipold, J. Madsen, D. Moseev, S. Nielsen, M. Nocente, T. Odstrčil, J. Rasmussen, L. Stagner, M. Stejner, M. Weiland, and the ASDEX Upgrade team. High-definition velocity-space tomography of fast-ion dynamics. *Nuclear Fusion*, 56(10):106024, 2016.

[32] T. H. Stix. Fast-wave heating of a two-component plasma. *Nuclear Fusion*, 15(5):737, 1975.

[33] J. Y. Hsu, V. S. Chan, R. W. Harvey, R. Prater, and S. K. Wong. Resonance Localization and Poloidal Electric Field due to Cyclotron Wave Heating in Tokamak Plasmas. *Phys. Rev. Lett.*, 53:564–567, Aug 1984.

[34] G. W. Hammett. *Fast ion studies of ion cyclotron heating in the PLT tokamak*. PhD thesis, Princeton University, 1986.

[35] R. Bilato, M. Brambilla, and Z. Jiang. Implementing zero-banana-width quasi-linear operator for fast ICRF simulations. *Journal of Physics: Conference Series*, 401(1):012001, 2012.

[36] R. Bilato and M. Brambilla. Toroidal trapping effects in the surface-averaged Fokker-Planck SSFPQL solver. *AIP Conference Proceedings*, 1580(1), 2014.

[37] M. Weiland. *Influence of RF heating and MHD instabilities on the fast-ion distribution in ASDEX Upgrade*. PhD thesis, LMU München, 2016.

[38] M. Brambilla and R. Bilato. Simulation of ion cyclotron heating of tokamak plasmas using coupled Maxwell and quasilinear-Fokker–Planck solvers. *Nuclear Fusion*, 46(7):S387, 2006.

[39] J. Wright, P. Bonoli, M. Brambilla, F. Meo, E. D'Azevedo, D. Batchelor, E. Jaeger, L. Berry, C. Phillips, and A. Pletzer. Full wave simulations of fast wave mode conversion and lower hybrid wave propagation in tokamaks. *Physics of Plasmas*, 11(5):2473–2479, 2004.

[40] R. Bilato, M. Brambilla, E. Fable, and E. Poli. Direct toroidal torque driven by ICRF heating and its dependence on the plasma rotation. *Nuclear Fusion*, 57(7):076017, 2017.

[41] A. N. Tikhonov and V. I. Arsenin. *Solutions of ill-posed problems*. Vh Winston, 1977.

[42] A. N. Tikhonov and A. Goncharsky. Ill-posed problems in the natural sciences. *Ill-posed problems in the natural sciences, Moscow: MIR Publishers, 1987, 344 p., Advances in science and technology in the USSR. Mathematics and mechanics series*, 1, 1987.

[43] M. Anton, H. Weisen, M. J. Dutch, W. von der Linden, F. Buhlmann, R. Chavan, B. Marletaz, P. Marmillod, and P. Paris. X-ray tomography on the TCV tokamak. *Plasma Physics and Controlled Fusion*, 38(11):1849, 1996.

[44] R. Harvey, Y. V. Petrov, D. Liu, W. Heidbrink, G. Taylor, and P. Bonoli. NBI and HHFW Fast Ion Temporal Dynamics Modeling with CQL3D-Hybrid-FOW in NSTX Discharges. In *25th IAEA Fusion Energy Conference, St. Petersburg, Russia*, 2014.

[45] Y. V. Petrov and R. Harvey. A fully-neoclassical finite-orbit-width version of the CQL3D Fokker–Planck code. *Plasma Physics and Controlled Fusion*, 58(11):115001, 2016.

[46] P. A. Schneider, H. Blank, B. Geiger, K. Mank, S. Martinov, F. Ryter, M. Weiland, A. Weller, and the ASDEX Upgrade Team. A new compact solid-state neutral particle analyser at ASDEX Upgrade: Setup and physics modeling. *Review of Scientific Instruments*, 86(7), 2015.